CHEMISTRY OF MATERIALS

pubs.acs.org/cm

Article

Cooperative Lithium Sorption in Doped Layered Double Hydroxides Is Modulated by Colloidal (Dis)Assembly

Michael L. Whittaker,* Wenming Dong, Kai Li, Tolga Aytug, Sam F. Evans, Harry M Meyer III, Bruce A. Moyer, and Mariappan Parans Paranthaman

Cite This: *Chem. Mater.* 2023, 35, 3931−3940

Read Online

ACCESS | Metrics & More | Article Recommendations | Supporting Information

ABSTRACT: Lithium−aluminum layered double hydroxides (LDHs) selectively sorb lithium from brines, concentrating and purifying this critical element for subsequent conversion to active battery components. Lithium ion partitioning into lattice vacancies within the LDH structure is selectively enhanced with iron doping. However, this process leads to a highly coupled set of intercalation interactions whose mechanisms are challenging to assess in situ. Here, we show that iron modulates the size- and shape-dependent composition of LDHs and imposes a powerful control on lithium sorption processes in complex fluids. We observe fundamental units of LDH layers and aluminum ferrihydrite nanoclusters that (dis)assemble to form at least five distinct particle types that influence LDH lithium capacity and cyclability. Importantly, lithium sorption is controlled by feedbacks arising from the dynamic interconversion of planar stacks and scrolls of LDH layers, which exchange lithium, water, and other species in the process of (un)rolling due to similar energy scales of hydration, sorption, and deformation. Under appropriate iron redox conditions, the cycling efficiency and stability of lithium sorption can be optimized for the range of lithium concentrations found in many natural brines.

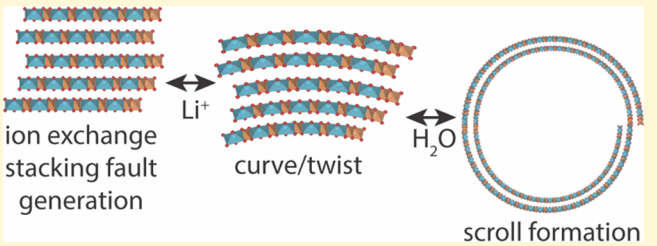

INTRODUCTION

Lithium is an integral element in high-energy-density batteries, and the separation of lithium compounds from brine resources is expected to be a key process for battery supply chains.[1] Sorbent materials such as layered double hydroxides (LDHs) are promising candidates for primary lithium extraction from geothermal brines because the sorption mechanism operates at the elevated temperatures of the brine and does not require pH swings to induce ion exchange,[2,3] thereby limiting sorbent degradation and chemical consumption relative to competing technologies such as ion-exchange resins.[4] However, brine compositions can vary dramatically over time and depend on extraction location.[4,5] When many chemical components are involved in the sorption process, as they often are for LDH, aqueous chemical variability alters the lithium activity in both aqueous and solid media, modulating lithium selectivity in poorly understood ways.

Doping lithium−aluminum LDH (Li/Al-LDH) with iron (Fe-LDH, up to approximately 30% iron on cation lattice sites with the balance in all cases being a mixture of Li and Al) has proven to thermodynamically stabilize the structure, counteracting the destabilizing effect of lithium sorption.[3] However, the complex interactions taking place between lithium sorption, iron doping, chlorine charge compensation, and ion/mineral hydration[6,7] are difficult to disentangle from the perspective of any individual component. Importantly, the stability[8] and lithium selectivity[2,3] of Fe-LDH are inconsistent with Langmuir sorption isotherm models that hold for Li/Al-LDH without iron.[9,10] More generally, the feedbacks between many different components that naturally occur in geothermal brines can give rise to distinct behavior from individual constituents observed in isolation.[11] This suggests that understanding cooperative effects between many components, both in the brine and in the sorbent material, is essential to understanding and controlling lithium sorption from complex brines.

Here, we directly and simultaneously investigate the atomic and colloidal structure of hydrated Fe-LDH using cryogenic electron microscopy (cryoEM) and cryogenic electron tomography (cryoET) and show that multiple coexisting phases control the overall lithium chloride (LiCl) and water sorption behavior in these materials. Results revealed the importance of understanding structural variability in poorly crystalline sorbents and controlling competing and parasitic reactions that result from chemical segregation. We found that chemical composition and hydration enthalpy systematically depend on the size and morphology of Fe-LDH particles.

Received: January 11, 2023
Revised: April 10, 2023
Published: May 3, 2023

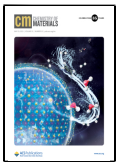

Observations revealed that (de)hydration, (de)intercalation, and (dis)assembly, such as faulted stacking and particle aggregation, alter the degree of (dis)order among the structural groups and ultimately define the bulk sorption behavior in these materials.

RESULTS

X-ray Diffraction. Fe-LDH has an X-ray diffraction (XRD) pattern that can be indexed to a monoclinic structure[2] with $C2/m$ symmetry and a = 4.88 Å, b = 5.32 Å, c = 15.29 Å, $\beta = \alpha = 90°$, and γ = 116.66° in either $1M_1$ or $1M_2$ polytypes. This structure can form from the faulted stacking of dritsite, a mineral with similar chemical composition and $P6_3/mcm$ symmetry (2H polytype), and its synthetic analogues that are derived by doping the $Al(OH)_3$ minerals gibbsite or bayerite[12−14] with lithium. Within the synthon framework proposed by Britto and Kamath,[13] shifting adjacent mineral layers of dritsite by ($^1/_3$, 0, z), (0, $^1/_3$, z), or ($^2/_3$, $^2/_3$, z) produces the $1M_1$ polytype via stacking faults that disorder the aluminum, iron, and lithium cations along the c axis of the unit cell. Shifts of ($^2/_3$, 0, z), (0, $^2/_3$, z), or ($^1/_3$, $^1/_3$, z) produce the $1M_2$ polytype via a related set of layer translations. Other sets of layer translations or rotations produce an unbounded set of stacking symmetries that vary continuously in directions orthogonal to the stacking vector. These shifts are distinguished from those of Bookin and Drits[15−18,17,18] which describe (pseudo)single cation sheets but do not account for cation disorder produced by, e.g., Li (de)sorption.

Anisotropic broadening of XRD peaks was observed between predominantly intra- or interlayer reflections[13] for Fe-LDH. These peaks are consistent with the coexistence of $1M_1$, $1M_2$, and possibly other faulted polytypes (Figure S1). Differences in relative peak intensities indicate differences in symmetries specifically related to cation ordering along the stacking axis between Fe-LDH and Li/Al-LDH (Figure S1).[17,18] For this reason, we could not uniquely determine the cell or cells present in our samples using the DIFFaX module of GSAS-II. We instead focused on complementary methods that illuminate this issue from different perspectives.

Differences in absolute intensities between Fe-LDH and Li/Al-LDH, including small-angle scattering from particle mesostructures, suggest that these different crystallographic symmetries give rise to distinct particle morphologies and distributions. However, cation disorder arising from ion exchange is difficult to distinguish from disorder arising from faulted stacking in bulk powder diffraction, especially when these types of disorder coexist (as they may be actively (de)sorbing materials). We have explored the relative contributions of layer rotation and/or translation vs ion exchange in greater detail using ambient secondary electron scanning electron microscopy (SE-SEM), cryoEM, and cryoET. The observed structures were correlated with chemical and thermodynamic measurements to better understand the complex microscopic LDH sorption mechanisms.

Electron Microscopic Imaging. Electron microscopic investigation of Fe-LDH revealed a distinct hierarchy of particle morphologies (Figures 1 and S2−S5). Complementary chemical, structural, and thermodynamic analyses confirm that morphological classes are associated with unique compositions that evolve differently during (de)sorption of water and LiCl. Plate-like and scroll-like aggregates are the principal morphologies discerned from SE-SEM (Figure 1a−c). These

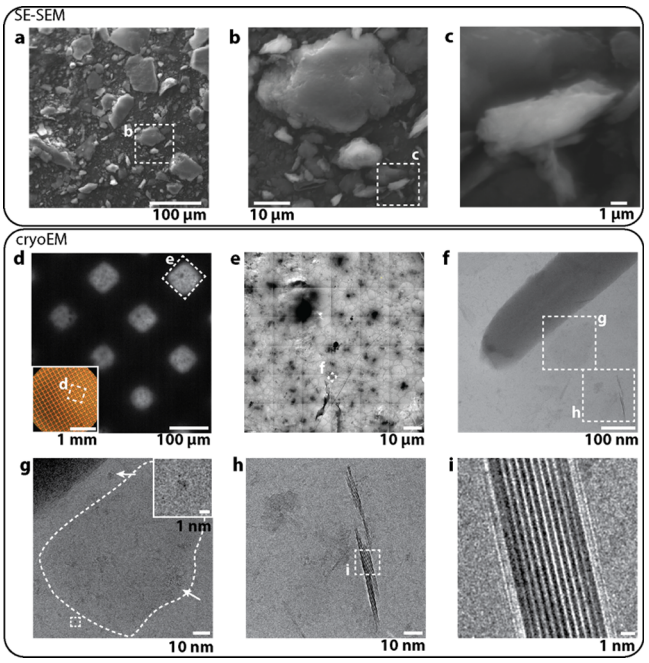

Figure 1. Electron microscopic imaging of Fe-LDH over six orders of spatial magnitude. Low-magnification SE-SEM images of (a) as-synthesized Fe-LDH aggregates, comprising (b) large plate-like aggregates and (c) smaller scroll-like aggregates. CryoEM images of (d) vitrified suspension at low magnification within copper squares of a transmission electron microscopy (TEM) grid on which Fe-LDH was plunge-frozen (optical image, inset). (e) Montage of low-magnification cryoEM images covering a single grid square in (d), showing large aggregates, scrolls, faceted plates, twisted plates, and many smaller particles. (f) Enlarged image of the nanoscroll tip. (g) Single Fe-LDH plate viewed face-on near the scroll edge, decorated in clusters of ∼2-nm particles (inset and arrow), which are also observed in the bulk solution. (h) Fe-LDH stack edge-on revealing (i) 3 Å thick layers and associated 0.7 Å interlayer space.

particles disaggregate upon resuspension and sonication in water (as discussed in Experimental Methods), revealing the presence of fundamental constituent units at smaller scales.

The true phase assemblage of Fe-LDH, identified and characterized in aqua with low-dose cryoEM and cryoET, consists of at least five morphological classes of these fundamental units at the nanoscale. Most of these classes do not diffract strongly because of their poorly crystalline or nanoparticulate structure. However, all structures play key roles in the bulk sorption behavior of Fe-LDH because their small sizes enable large active areas where sorption and (dis)assembly can occur.

Low-magnification cryoEM images (Figures 1d and S2−S5) revealed aggregates of particles with maximum dimensions consistent with those observed in SE-SEM (Figure 1e). However, two fundamental structural units observed in cryoEM at smaller scales comprise the larger particle aggregates. The LDH layer, which is the primary structural unit identified via XRD, was found as either free suspended layers with approximately 3.0 Å thickness (±2 standard deviations for edge-on layers, Figure 1h), planar platelets with 3.77 Å fundamental interparticle spacing along the stacking direction (Figures 1h,i and 2), or rolled nanoscrolls (Figure 1e,f).

Imaging plate-like particles face-on (Figures 1f,g and 2a−c) revealed that the threefold symmetry of the LDH layer was

https://doi.org/10.1021/acs.chemmater.3c00072
Chem. Mater. 2023, 35, 3931−3940

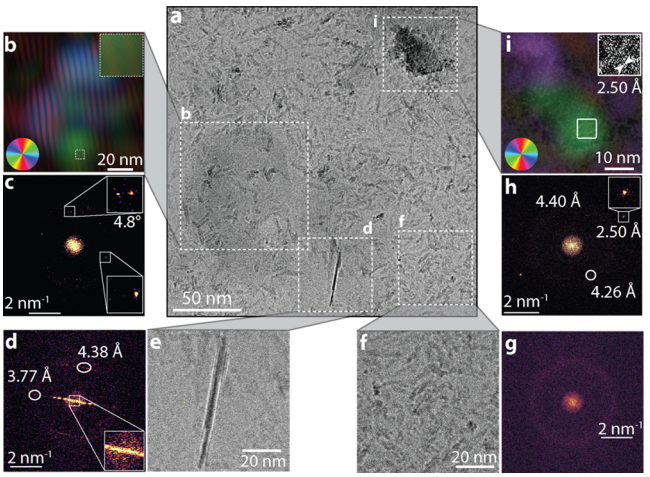

Figure 2. Particle morphologies in suspension viewed with low-dose cryoEM. (a) Overview image of suspension with nanoscale particles. (b) Face-on stack exhibiting lattice spacings consistent with faulted Fe-LDH, including a low-angle Moiré superlattice. The color wheel depicts false coloring by Bragg filtering the (c) fast Fourier transform (FFT), which shows split spots along specific directions. (d) Edge-on stack of up to five layers, also consistent with disordered faulted Fe-LDH, as seen in the (e) FFT, depicting the stacking vector direction (inset). (f) Non-crystalline rough prolate spheroidal ferrihydrite particles, with (g) no strong crystallinity at spatial scales above the low-dose imaging resolution of approximately 2.2 Å. (h, i) Ferrihydrite cluster with two highly crystalline domains that span multiple smaller units but are misaligned with respect to each other.

broken when stacked. This phenomenon is associated with the misalignment of at least one of the three principal layer directions by small angles (e.g., 4.8°, Figure 2c), which produces a Moiré superlattice with a periodicity of approximately 2 nm in a subset of the observed layers. Overlapping regions of superlattice misalignment with crystallographically aligned domains of approximately 20−50 nm produced a complex stacking pattern that gives rise to a broad distribution of faulted stacking order across and between the layers (Figure 2b).

Layers oriented edge-on exhibit multilayer stacking sequences of two, three, four, and five layers, corresponding to integer multiples of the fundamental 3.8 Å spacing. Stacking periodicity can also be misaligned from the direction normal to the layer by up to 5° (Figure 2d,e), which is consistent with disordered stacking that is exclusively due to the rotational disorder of layers and not to the cation disorder among layers that are otherwise stacked crystallographically. Therefore, the higher degree of disordered layer stacking relative to undoped Li/Al-LDH can explain the observed reduction in Fe-LDH diffraction intensity. In other words, crystalline domains that diffract coherently in Fe-LDH are continuously distributed among a variety of polytypic sequences and represent only a fraction of the total particle volume.

Faulted stacking is an intermediate state between well-crystalline Li/Al-LDH and nanoscrolls observed in Figure 1e,f. Transition states between the planar and scrolled particles were observed in microscopic proximity to both of these structures throughout the suspension in hundreds of separate and specific instances (Figures 3 and S2−S4), strongly suggesting that plates and scrolls dynamically interconvert by (un)rolling. The process of (un)rolling involves curvature that develops in response to asymmetric bending strain across the layers,[19] which may be driven by heterogeneous ion exchange between layers with different degrees of misalignment, different extents of exchange (i.e., chemical heterogeneity), or different interfacial hydration states.[20−22] Furthermore, particle dimensions change dramatically as layers (un)roll. Scrolls with lengths of hundreds of micrometers coexist with layers whose maximum dimension does not exceed a few nanometers, suggesting that scrolls (dis)assemble from smaller plate-like units. These morphological transitions appear to be coupled to lithium and iron(II) (de)sorption as well as to the irreversible loss of iron(III), both of which have important implications for the capacity and cyclability of lithium sorbents.

A second population of rough prolate spheroidal nanoclusters—clearly distinct from Fe-LDH layers—with a relatively monodisperse size distribution of approximately 2 nm diameter and 5 nm length was pervasive throughout the solution, as observed by cryoEM (Figure 2a,f−i). These particles were found to be isolated in suspension, aggregated near the edges of plates and scrolls, and in dense partially crystalline aggregates (Figures 1g and 2f). Individually, the primary nanoclusters do not exhibit strong lattice fringes (Figure 2f,g) but adopt long-range order when aggregated (Figure 2h,i). Fourier transforms of cryoEM images (Figure 2a,h,i) containing these nanoparticle aggregates reveal sharp periodic features at 2.50, 4.26, and 4.40 Å that are consistent with distinct domains of well-crystalline ferrihydrite.[23] Therefore, the primary particles are poorly crystalline ferrihydrite, and the process of aggregation triggers the development of long-range order. These conclusions are consistent with

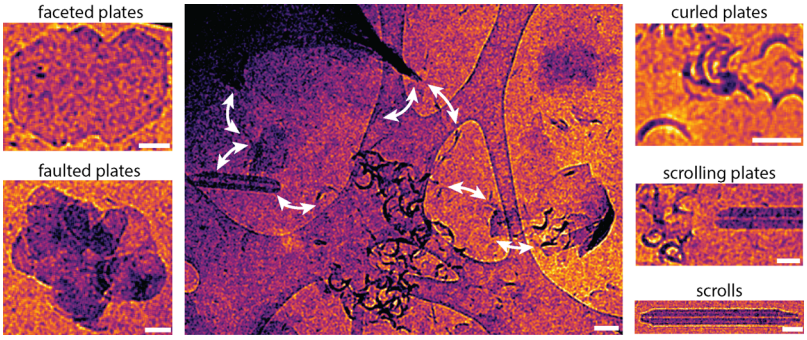

Figure 3. Interconverting Fe-LDH particle morphologies in suspension viewed with low-dose cryoEM. A variety of LDH particle types coexist in Fe-LDH suspensions, many of which are actively transforming between different morphologies. Thousands of similar examples are observed (Supporting Information), supporting the pervasive nature of these phenomena. Scale bars represent 100 nm.

https://doi.org/10.1021/acs.chemmater.3c00072
Chem. Mater. 2023, 35, 3931−3940

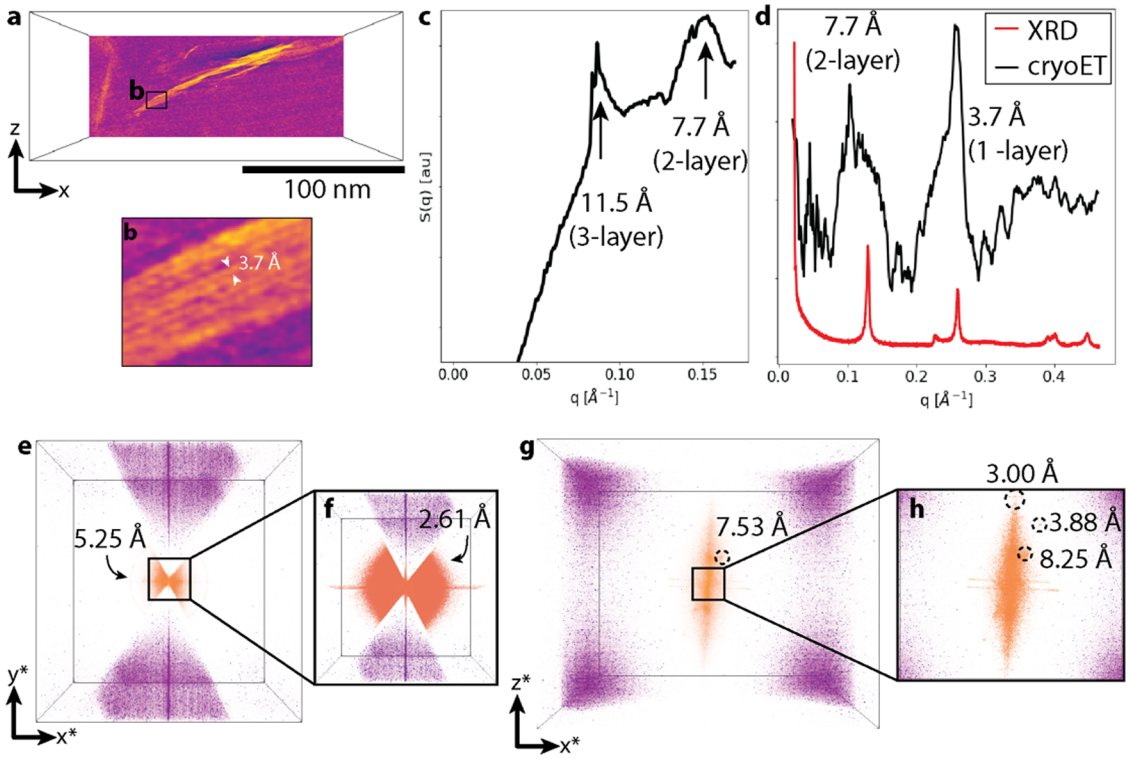

Figure 4. CryoET of LDH tactoid in real and reciprocal space. (a) Slice in the $x-z$ plane of the 3D volume rendering of an Fe-LDH tactoid in suspension showing the aqueous solution (dark), tactoid (light), and other suspended nanoparticles. (b) Inset of the region in (a) showing the 3.7 Å interlayer spacing normal to the stacking direction. (c) Fourier downsampled $S(q)$ at low q. (d) $S(q)$ of (a) at full resolution and comparison with XRD. (e–h) 3D Fourier transforms of (a), revealing Bragg spots that correspond to stacking sequences and layer orientations.

previous observations[24] and mechanistic predictions of ferrihydrite transformation pathways[23,25] toward more stable phases such as hematite, but they appear to be the first observations of such a direct transformation between putative ferrihydrite structures.

CryoET. The Fe-LDH polytypism suggested by cryoEM imaging was elucidated in 3D via cryoET (Figure 4) (Figures S3–S5). A 245 × 440 × 98 nm volume containing approximately 23 layers stacked into a tactoid was reconstructed to 2.2 Å resolution. Individual Fe-LDH layers and the interlayer space between them were resolved across disordered stacking regions that were generally also curved (Figure 4a–c). Real-space reconstructions had relatively low signal-to-noise ratios because of the low-dose imaging methodology employed to preserve hydrated cryo-frozen structures (as discussed in Experimental Methods). Therefore, the 3D Fourier transform of the reconstructed volume (Figure 4h–l) and its volumetric integral (Figure 4d,e) were used to determine the cryoET structure factor, $S_c(q)$. A similar technique has been applied to understand the radial distribution of ferrihydrite particles but has not been demonstrated with lattice resolution in order to index diffraction peaks, to our knowledge.[26]

The $S_c(q)$ recapitulates the dominant features of the LDH XRD pattern over comparable scattering vectors, q, that arise from the stacking of individual LDH layers approximately 3.0 Å thick with 0.7 Å interlayer space. However, key differences between XRD and $S_c(q)$ reveal local structural defects within individual tactoids that corroborate the crystallographic disorder observed in Figure 2 and have significant consequences for lithium sorption capacity and selectivity.

One-, two-, and three-layer stacking motifs are observed in the $S_c(q)$, corresponding to basal spacings of 3.7, 7.7, and 11.5 Å (Figure 4d,e) within stacked domains of 10–15 layers. The stacking vector varies between the normal to the plane of the layer and a maximum of approximately 115° relative to the $x-y$ plane (Figure 4h–l). The approximately 5.25 Å lattice parameters of each individual layer, corresponding to the distance between non-adjacent cation sites, and the 2.61 Å distance between adjacent cations are distributed isotropically around the stacking axis (Figure 4h,i), indicating that no long-range orientational ordering exists among layers across a tactoid.

Importantly, the Fourier components from the 2D projection images in Figure 2b–e, such as the 4.38 Å lattice parameter in Figure 2c, are the result of diffraction phenomena that encode atomic structural information. The multi-defocus tilt series scheme[19,27,28] that was employed to reconstruct 3D volumes (as discussed in Experimental Methods) allows for the direct determination of lattice positions, free of encoded phase inversion effects. Therefore, this scheme provides a clearer picture of the true stacking sequence of Fe-LDH layers. Taken together with the disordered stacking observed in 2D images of five or fewer layers (Figure 2a–e), these observations indicate that stacking faults associated with ordered and disordered polytypes coexist within the same tactoid and persist along the stacking direction for only a few layers (1–2 nm) within a 20–50 nm local region within the plane of a layer before a distinct stacking motif prevails. Thus, even in the same interlayer space (or on opposite sides of the same layer), the chemical environment varies from the perspective of an exchanging ion (such as lithium) or a water molecule.

https://doi.org/10.1021/acs.chemmater.3c00072
Chem. Mater. 2023, 35, 3931–3940

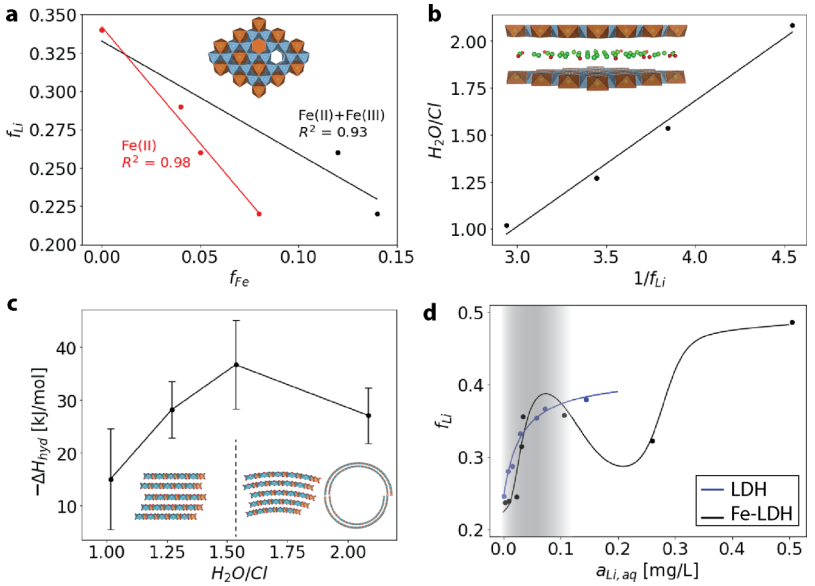

Figure 5. Coupled sorption chemistry in Fe-LDH. (a) Fraction of cation sites occupied by lithium as a function of the iron fraction. (b) Linear relationship between the inverse lithium fraction and the number of water molecules per interlayer chloride ion. (c) Non-monotonic dependence of the average hydration enthalpy on the hydration state of interlayer chloride. Error bars represent one standard deviation over measurements taken at 10% relative humidity intervals (Figure S7). (d) Sorption isotherms for Li/Al-LDH and Fe-LDH, with typical lithium contents in geothermal brines[31] highlighted.

Chemical Segregation. Size fractionation of Fe-LDH suspensions via centrifugation revealed important chemical differences among the different morphological classes of particles (Figure S6). Aggregates of nanoscrolls and large stacks of LDH layers comprise the densest fraction, smaller stacks of LDH layers and ferrihydrite aggregates have a relatively lower density, and primary ferrihydrite particles and exfoliated LDH layers comprise a fraction that maintains colloidal stability in aqueous solution. Energy-dispersive spectroscopy (EDS) and inductively coupled plasma–mass spectrometry (ICP-MS, Tables S1 and S2) suggest a nominal overall composition of $Li_{0.29}Al_{0.59}Mg_{0.01}Fe_{0.12}(OH)_3Cl_{0.37}\cdot nH_2O$ for as-synthesized Fe-LDH, where n = 0.47 is the maximum molar water content determined by isothermal hydration gravimetry and calorimetry (IHGC) analysis (Figures S7–S9). IHGC determines the heat flow and associated mass change due to the addition or removal of water from nearly 0% relative humidity to nearly 100%, from which the molar enthalpy change can be determined. Fe-LDH had a lower total water content compared with Li/Al-LDH, which had a composition of $Li_{0.34}Al_{0.66}Mg_{0.01}(OH)_3Cl_{0.55}\cdot 0.56H_2O$. The densest fraction was depleted in lithium and iron and contained slightly more water: $Li_{0.22}Al_{0.63}Fe_{0.14}Mg_{0.01}(OH)_3Cl_{0.21}\cdot 0.49H_2O$. However, a gravimetrically lighter sedimented fraction was highly depleted in iron and contained a higher amount of lithium and less water: $Li_{0.26}Al_{0.69}Fe_{0.04}Mg_{0.01}(OH)_3Cl_{0.28}\cdot 0.43H_2O$.

X-ray photoelectron spectroscopy (XPS) analysis confirmed that iron was initially present in both 2+ and 3+ redox states. The proportion of iron(II)/iron(III) (Figure S10) was consistent with the distribution of iron across both aluminum (iron(III)) and lithium (iron(II)) lattice sites in the Fe-LDH structure (Figure 4a). ICP-MS, EDS, and XPS also revealed the presence of a small amount of magnesium, which appeared to reside on lithium lattice sites. Accordingly, the net layer charge was compensated by a proportional amount of chlorine interlayers and quantitatively could be determined directly from the mole fractions of cations according to

$$x_{Cl} \cong x_{Li} + 2(x_{Fe} - (0.66 - x_{Al})) - x_{Mg} \quad (1)$$

Thus, lithium, iron(II), and magnesium directly compete for lattice sites in the Fe-LDH structure, which is consistent with previous reports on LDHs (e.g., green rust[6,7]).

The excess charge imparted by iron(II) intercalation alters the strength of interactions between Fe-LDH layers and other interlayer species, such as chlorine and water. These modified interlayer interactions are hypothesized to cause the disordered stacking and morphological transformation that was observed in our samples (Figures 123). The fraction of lithium in the lattice was inversely proportional to the number of water molecules per chlorine anion in the interlayer (Figure 5b), with a higher lithium content corresponding to fewer water molecules per chloride ion. Likewise, more iron(II) decreases the number of water molecules per chlorine anion.

Hydration. The average hydration enthalpy per water molecule as determined by IHGC was observed to increase in magnitude with the increase in the total water content, except for the densest size fraction containing scrolled particles (Figures 5c, S9, and S10). Not only was more water present as the charge on the layers increased, but each water molecule was more tightly bound, on average, as evidenced by a more exothermic enthalpy of adsorption. The size fraction that contained scrolled particles had a slightly less exothermic water adsorption enthalpy despite having the highest water content, which is consistent with surfaces that become more hydrophilic as the degree of curvature increases.[29] Together with chemical analysis, IHGC results suggest that increasing the iron(II) content strengthens water–anion–LDH interactions. Previously obtained calorimetry[3] assessing the formation enthalpy of hydrated Fe-LDH has shown that Fe-LDH structures are more stable with less water for nearly equivalent lithium and iron contents, which is consistent with the overall

https://doi.org/10.1021/acs.chemmater.3c00072
Chem. Mater. 2023, 35, 3931–3940

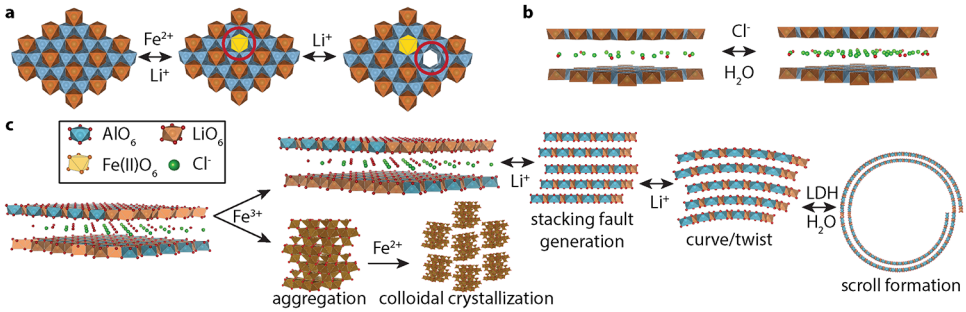

Figure 6. Conceptual picture of coupled chemical and mechanical sorption processes in the Fe-LDH system. (a) Ion exchange within the Li/AL-LDH sheet. The red circle indicates vacancy created by Li desorption. (b) Water sorption in the interlayer. (c) Chemical−mechanical processes contributing to sorption and segregation across spatial scales.

trend of decreasing water sorption enthalpies with increasing relative humidity measured here (Figure S9). Therefore, there is a competition between the increasing favorability of water sorption with increasing charge, increasing stability with increasing iron content, and decreasing stability with increasing water content at constant charge that is difficult to reconcile without accounting for changing particle structures as lithium (de)sorbs.

Cooperative Effects on Lithium Sorption. Lithium sorption tests were performed to compare the equilibrium lithium uptake of Fe-LDH with that of Li/Al-LDH and assess the role of morphological evolution and chemical segregation. Bench-scale sorption tests using synthetic lithium-containing brine solutions confirmed that Fe-LDH had a similar sorption capacity to Li/Al-LDH over the range of lithium concentrations found in geothermal brines (Figure 5d). However, although the lithium sorption mechanism in Li/Al-LDH is consistent with a Langmuir adsorption isotherm, the Fe-LDH sorption mechanism was found to be qualitatively different. A sharp transition between loaded and unloaded states can be modeled with a cooperative-binding sorption isotherm[30] that is modified to account for the destabilizing effect of lithium intercalation on the Fe-LDH free energy (Supporting Information).

The Langmuir adsorption isotherm that describes lithium sorption in LDH without iron does not capture many aspects of Fe-LDH sorption. Specifically, Langmuir sorption decreases monotonically as the fraction of occupied lithium sites increases, while the Fe-LDH data exhibit three points of inflection. Two of these inflection points at aqueous lithium activities below 0.2 mg/L are well described by the cooperative sorption isotherm.[30] The third inflection point captures the increase in sorption capacity at lithium activities above 0.2 mg/L. Although the presence of this third inflection point depends very sensitively on the fitting parameters, its presence is highly motivated by previous thermochemical studies of Fe-LDH showing the competing effects on the formation and hydration enthalpies of Fe-LDH.[3]

The fraction of cation lattice sites that are occupied by lithium, f_{Li}, can be determined using a three-parameter cooperative sorption model[30] that is modified to include the known decrease in Fe-LDH formation enthalpy with decreasing iron content:

$$f_{Li} = \frac{1 + A_1 + A_m}{A_1 + mA_m} \frac{A_1 x + mA_m x^m}{1 + A_1 x + A_m x^m} \quad (2)$$

where A_1 is the first-order expansion coefficient of the sorption polynomial, A_m is the mth-order coefficient, assumed to have a dominant effect on the cooperativity, and x is the aqueous activity of lithium. Because lithium competes with iron(II) in the Fe-LDH lattice, increasing the aqueous lithium activity is assumed to have both positive and negative feedbacks on the lithium content of the sorbent. These feedbacks are incorporated by expressing A_m as

$$A_m = A_o e^{kT\Delta\mu_{Li}} \quad (3)$$

where A_o is a fitting parameter and $\Delta\mu_{Li}$ is approximated from the empirical lithium dependence of the formation enthalpies of Li/Al-LDH and Fe-LDH determined previously.[3] Thus, combining eqs 2 and 3 yields the fit shown in Figure 5d.

In this cooperative sorption model, individual sorption events are not independent and do not occur on a static free-energy landscape but instead occur collectively and change the free-energy landscape as they occur. This observation contrasts with the Langmuir isotherm in which individual sorption events are considered to be independent, but it is completely consistent with the disordered molecular assemblies evinced by cryoEM and cryoET imaging. We note that eq 2 reduces to the Langmuir model in the absence of cooperativity ($A_m \to 0$, $\Delta\mu_{Li} \ll 0$). Remarkably, the strong switching between loaded and unloaded states falls within the range of lithium concentrations found in natural geothermal brines and indicates that Fe-LDH cycling is much more sensitive than undoped LDH cycling over technologically relevant conditions.

DISCUSSION

The magnitude of the hydration enthalpy per mole of water for Li/Al-LDH and Fe-LDH (Figures 5c and S9), based on the number of water molecules per formula unit, is on the same scale as the formation enthalpy[3] per formula unit. Furthermore, the observed hydration enthalpy increases with increasing iron content, and we hypothesize that the presence of iron(II) in lithium lattice sites, and the greater net charge it imparts, increases the net electrostatic attraction between layers and interlayer species. This is consistent with the linear dependence of the interlayer water content on the inverse of the lithium fraction (Figure 5b). Because the lithium content is itself inversely proportional to the iron content, increasing the iron(II) content appears to recruit more water to reside in the interlayer space to screen repulsive interactions between interlayer anions or structural charge sites on adjacent LDH layers. Thus, the addition of iron to Li/Al-LDH creates a highly coupled set of interactions between nearly all the

https://doi.org/10.1021/acs.chemmater.3c00072
Chem. Mater. 2023, 35, 3931−3940

constituents in the Fe-LDH system that are not easily disentangled. This suggests that cooperative mechanisms may be used to tune the lithium selectivity of sorbents for a particular range of concentrations, or a specific impurity profile, for greater control over sorption selectivity and efficiency.

Comparable hydration and formation enthalpies indicate that a change in the hydration state, such as that accompanied by the exchange of lithium or iron within the layer and the concomitant interlayer exchange of hydrated chlorine, is sufficient to dramatically alter the (Fe-)LDH structure. The mechanisms by which this structural modification occurs are detailed in Figure 6. At the smallest scales, ion exchange in the Li/AL-LDH lattice alters the net charge on the lattice. Variable lattice charge alters the chlorine and water content in the interlayer. If layers are free to translate and rotate, as they are in Fe-LDH, asymmetrical and disordered stacking among Li/Al-LDH layers leads to the curling up of highly defective stacks due to the imbalance of forces across a layer or tactoid. The loss of iron(III) may occur at different stages along this process, but the ultimate consequence of iron(III) segregation is the formation of non-crystalline prolate spheroid ferrihydrite particles (Figure 2f,g) that aggregate into crystalline ferrihydrite with long-range order spanning many individual particle domains. The as-synthesized Fe-LDH contains both iron(II) and iron(III), and the substitution of iron(III) for aluminum is not expected to alter the hydration enthalpy of LDH considerably,[6,7] so the formation of primary ferrihydrite particles is not likely to be a main control on the lithium sorption capacity of Fe-LDH. However, it has been shown that iron(II) sorbed on the surface of ferrihydrite particles can oxidize and promote crystallization.[32] This may represent a parasitic pathway for the loss of iron(II) from Fe-LDH if not suppressed but is likely self-limiting by the initial iron(III) concentration unless large changes in redox potential (e.g., pH) occur.

Sudare et al. show that LDH polytypes exhibit vastly different anion intercalation capacities and kinetics.[33] They attribute differences between $2H_1$ and $3R_1$ polytypes of Mg/Al LDH to lattice "rigidity". We interpret this observation as an example of the early stages of our model, as shown in Figure 6c, since the presence or generation of stacking faults was shown to create a fourfold increase in the anion sorption capacity. We interpret our model as continuing along this reaction coordinate in which decreasing lattice "rigidity" proceeds all the way through curling into scrolls, which carries such a high energetic cost that chemical alteration via dehydration and deintercalation occurs simultaneously. However, we note that the anion sorption behavior in Sudare et al. follows a Langmuir trend, which suggests that the cooperativity observed in Fe-LDH here arises from substantial layer curvature and not from stacking fault generation.

Macroscopic transformation between particle morphologies may have irreversible consequences for lithium sorption capacity. Indeed, we show that significant degradation occurs after just 48 h of operation at 100 °C (Figure S11). However, we show that the structure can be regenerated after incubating in a LiCl-rich solution for just 3 h (Figure S12), which demonstrates that the morphological changes observed upon lithium sorption, and the degradation that occurs at elevated temperatures, can be chemically reversed. This supports the inherent coupling between the solution chemistry and the particle morphology summarized in Figure 6 and offers strategies for preserving sorbent materials and increasing their cycle life under harsh conditions.

CONCLUSIONS

Supported by thermochemistry and chemical analysis, cryoEM and cryoET were used to survey the naturally present heterogeneity in Fe-LDH suspensions. In particular, the high-resolution information captured by the 2D projection images from cryoEM was combined with the 3D information obtained from cryoET reconstructions to elucidate the microscopic structures of Fe-LDH particles that cannot otherwise be discerned from bulk methods such as XRD. This information is crucial to understanding sorption mechanisms from a molecular perspective because the specific local energy landscape experienced by an ion or molecule arises only from local forces, such as the (mis)orientation of adjacent layers or the hydration state of an interlayer anion.

The Fe-LDH system's ability to morphologically adapt to changing aqueous solution conditions was found to enable highly selective lithium sorption characteristics because strong feedback exists between the layer chemistry and the morphology. Favorable lithium sorption sites may become unfavorable as proximate sites fill and then alter the nearby hydration of chloride ions or the stacking orientation of adjacent layers. This adaptable sorption in Fe-LDH allows what would otherwise be a competition between iron(II) and lithium for lattice sites to become a mechanism for enhanced selectivity by distributing these elements between a number of coexisting phases whose proportions and properties vary with changing conditions. These observations not only elucidate key mechanisms governing the selective separation of one of the most important elements of 21st-century energy-storage systems but also reveal general paradigms for improving selective sorption via hierarchical systems-level understanding of sorbent behavior.

EXPERIMENTAL METHODS

Synthesis. The Fe-LDH samples were synthesized via a hydrothermal process as reported previously.[3] Lithium hydroxide ($LiOH{\cdot}H_2O$, 62.94 g), aluminum hydroxide ($Al(OH)_3$, 234 g), and ferric chloride hexahydrate ($FeCl_3{\cdot}6H_2O$) (Sigma-Aldrich, >97%) were mixed in a stainless-steel container with 1 L deionized (DI) water. The mixture was stirred (350 rpm) and heated at 95 °C in the Paar reactor for 36 h. Then, the resultant mixture was added to 720 mL LiCl solution (67.8 g of LiCl) and stirred for 1 h to exchange OH^- with Cl^- ions associated with Li^+. Acetic acid was added to maintain the pH of the solution above 5.5 during this process. After the ion-exchange step, the mixture was stirred for an additional 12 h at room temperature to allow for a complete reaction. The mixture was then centrifuged, washed with DI water, and air-dried. A brown product (220 g) was obtained. Li/Al-LDH was synthesized via a process similar to that of Fe-LDH without the addition of $FeCl_3$.

For lab/bench-scale sorption isotherm experiments (Table S4), both Li/Al-LDH and Fe-LDH samples were prepared as follows. Pure Li/Al-LDH samples were prepared by mixing $Al(OH)_3$ (Alfa Aesar, >76.5%) and LiOH (Honeywell Fluka, >98.5%) at 95 °C for 2 h. Then, the LDH structure was fully loaded with lithium by mixing it with 40% LiCl (Sigma-Aldrich, >99%) in an acetic acid (Sigma-Aldrich, >99.7%) and DI water mixture in a ratio of 6:4 mL, respectively. Complete LiCl loading of the structure was achieved when the solution's pH reached 5.5. Acetic acid was used as the buffer solution to maintain the pH close to 5. The Fe-LDH was prepared by adding $FeCl_3$ (Sigma-Aldrich, >97%) in 10 wt % loading to a heated mixture of $Al(OH)_3$ followed by LiOH to ensure proper mixing of the metals that would compose the layered hydroxide double layer with

https://doi.org/10.1021/acs.chemmater.3c00072
Chem. Mater. 2023, 35, 3931−3940

iron replacing some aluminum species. Upon completion of the doping process, Fe-LDH was mixed with a 40% LiCl acetic acid solution to fully load it with lithium. The LiCl was unloaded from these samples by heating to 95 °C and stirring for 1 h before sorption isotherm experiments were performed.

X-ray Diffraction. Li/Al-LDH and Fe-LDH were characterized by XRD using a Rigaku SmartLab diffractometer operating at 40 kV and 40 mA. Samples of 100 mg were pressed into 20 mm diameter pellets to a maximum pressure of 2 tons. The similarity in the scattering intensity at the smallest diffraction angles (1−3 °2θ) suggests similar density and packing of large particle aggregates. Differences in the mid- and large-angle (3−80 °2θ) diffraction intensity and peak position suggest differences in local particle stacking, layer composition, and defect structure between Fe-doped and Fe-free materials.

Size Fractionation. As-synthesized particles consisted of multiphase aggregates that dispersed in aqueous solution. Particles were ground by hand with a mortar and pestle and then resuspended in either milliQ water (resistivity = 18.2 MΩ cm) or 1 M LiCl at a concentration of 50 mg/mL. Then, they were sonicated with a Vibracell Ultrasonic processor at 2 W and 20 kHz, alternating 30s on, 30 s off for 30 min.

CryoEM/CryoET. Vitrified samples for cryo-imaging were prepared by depositing 1.5 μL to each side of a glow-discharged 200-mesh copper TEM grid with a lacy carbon support, blotting with a Vitrobot Mark IV automated freezing robot for 10 s with a force of 10, and plunge-freezing into liquid ethane. Samples were transferred to a Thermo Fischer Titan Krios G3i cryo-electron microscope equipped with a Gatan K3 direct electron-detecting camera operated in correlated double sampling and super-resolution modes and a bioQuantum energy filter with a 20 eV acceptance aperture on the direct beam. Data acquisition was automated with custom scripts written in SerialEM. Dose-fractionated single-particle cryoEM movies were acquired with a total dose of 100 electrons/Å^2 at a super-resolution pixel size of 0.6535 Å and a dose rate of 7.3 electrons/Å^{2}s. Tilt series were collected with a dose-symmetric acquisition scheme and three defocus values per tilt (−50, −250, and −1000 nm). Movies were aligned and particle classes were created with RELION 3.0. Tomographic reconstruction was performed in IMOD, analysis was performed using custom scripts in Python (Ren et al.[28]), and visualizations were created in TomViz.

Lab/Bench-Scale Testing. Fe-LDH and Li/Al-LDH samples for bench-scale sorption testing were dried at room temperature to retain bulk water in the structure. A standard synthetic brine was prepared with salt concentrations reflecting those in a reference geothermal brine containing 250 ppm of lithium (Table S3). Loading trials were performed at lithium concentrations varying from 0 to 7000 ppm, while other ion concentrations were held constant. The pH of the brine was measured to be 6 and was not adjusted. Bench-scale testing was performed by first unloading the Fe-LDH samples to make them deficient in lithium for sorption. This process was performed by adding 250 mg of the sorbent to 5 mL of DI water followed by heating and stirring for 1 h at 95 °C. After about 40% of the intercalated lithium had been removed, the sample was filtered and washed. Then, sorption testing was performed to determine an isotherm of loading capacities at a variety of lithium concentrations in the simulated brine.

Samples were characterized by XRD using a PANalytical Empyrean with Cu Kα radiation, and all data were processed with HighScore Plus. Inductively coupled plasma−optical emission spectroscopy compositional analysis was performed with a Thermo Fischer iCAP Model 7400 ICPOES Duo to determine the lithium and aluminum concentrations in all samples.

■ ASSOCIATED CONTENT

Supporting Information

The Supporting Information is available free of charge at https://pubs.acs.org/doi/10.1021/acs.chemmater.3c00072.

XRD and Rietveld refinement of the as-synthesized material, cryoEM montage and Bragg filtered images, EDS, isothermal hydration calorimetry, XPS (Fe), brine chemistry, column separation factors, cooperative sorption model, and XRD of stability and rejuvenation (PDF)

■ AUTHOR INFORMATION

Corresponding Author

Michael L. Whittaker − *Energy Geosciences Division and Materials Science Division, Lawrence Berkeley National Laboratory, Berkeley, California 94720, United States;* orcid.org/0000-0002-9724-3409; Email: mwhittaker@lbl.gov

Authors

Wenming Dong − *Energy Geosciences Division, Lawrence Berkeley National Laboratory, Berkeley, California 94720, United States*

Kai Li − *Chemical Sciences Division, Oak Ridge National Laboratory, Oak Ridge, Tennessee 37831, United States;* orcid.org/0000-0003-1445-3206

Tolga Aytug − *Chemical Sciences Division, Oak Ridge National Laboratory, Oak Ridge, Tennessee 37831, United States;* orcid.org/0000-0001-7971-5508

Sam F. Evans − *Chemical Sciences Division, Oak Ridge National Laboratory, Oak Ridge, Tennessee 37831, United States*

Harry M Meyer III − *Chemical Sciences Division, Oak Ridge National Laboratory, Oak Ridge, Tennessee 37831, United States*

Bruce A. Moyer − *Chemical Sciences Division, Oak Ridge National Laboratory, Oak Ridge, Tennessee 37831, United States;* orcid.org/0000-0001-7484-6277

Mariappan Parans Paranthaman − *Chemical Sciences Division, Oak Ridge National Laboratory, Oak Ridge, Tennessee 37831, United States;* orcid.org/0000-0003-3009-8531

Complete contact information is available at: https://pubs.acs.org/10.1021/acs.chemmater.3c00072

Author Contributions

M.L.W. conceived the study design, performed SE-SEM, cryoEM, cryoET, XRD, and IHGC experiments, analyzed data, and wrote the manuscript. E.C. performed XPS experiments. W.D. performed ICP-MS experiments. K.L., T.A., S.F.E., M.P.P., and B.M. performed bench-scale sorption experiments. M.P.P. conceived the study design.

Notes

The authors declare no competing financial interest.

■ ACKNOWLEDGMENTS

We thank Dan Toso for technical assistance with the FEI Titan Krios. We also thank Stephen Harrison for assistance with ICP analysis. This work was supported by the U.S. Department of Energy, Office of Science, Office of Basic Energy Sciences, Chemical Sciences, Geosciences, and Biosciences Division, through its Geoscience program at LBNL under Contract DE-AC02-05CH11231. Synthesis of LDH and Fe-doped LDH sorbents was supported by the U.S. Department of Energy, Office of Energy Efficiency and Renewable Energy, Office of Geothermal Technologies Office through a Technology

Commercialization Fund. Bench-scale column extraction research was supported by the Critical Materials Institute, an Energy Innovation Hub funded by the U.S. Department of Energy, Office of Energy Efficiency and Renewable Energy, Advanced Materials and Manufacturing Technologies Office. This manuscript has been authored by UT-Battelle, LLC under Contract No. DE-AC05-00OR22725 with the U.S. Department of Energy. The United States Government retains and the publisher, by accepting the article for publication, acknowledges that the United States Government retains a non-exclusive, paid-up, irrevocable, worldwide license to publish or reproduce the published form of this manuscript, or allow others to do so, for United States Government purposes. The Department of Energy will provide public access to these results of federally sponsored research in accordance with the DOE Public Access Plan (http://energy.gov/downloads/doe-public-access-plan).

REFERENCES

(1) Hund, K.; La Porta, D.; Fabregas, T. P.; Laing, T.; Drexhage, J. *Minerals for Climate Action: The Mineral Intensity of the Clean Energy Transition*; World Bank, 2020.
(2) Paranthaman, M. P.; Li, L.; Luo, J.; Hoke, T.; Ucar, H.; Moyer, B. A.; Harrison, S. Recovery of Lithium from Geothermal Brine with Lithium−Aluminum Layered Double Hydroxide Chloride Sorbents. *Environ. Sci. Technol.* **2017**, *51*, 13481−13486.
(3) Wu, L.; Li, L.; Evans, S. F.; Eskander, T. A.; Moyer, B. A.; Hu, Z.; Antonick, P. J.; Harrison, S.; Parans Paranthaman, M.; Riman, R.; Navrotsky, A. Lithium Aluminum-layered Double Hydroxide Chlorides (LDH): Formation Enthalpies and Energetics for Lithium Ion Capture. *J. Am. Ceram. Soc.* **2019**, *102*, 2398−2404.
(4) Stringfellow, W. T.; Dobson, P. F. Technology for the Recovery of Lithium from Geothermal Brines. *Energies* **2021**, *14*, 6805.
(5) Warren, P. *Techno-Economic Analysis of Lithium Extraction from Geothermal Brines*; NREL/TП−5700−79178 ; National Renewable Energy Laboratory (NREL), 2021.
(6) Ruby, C.; Abdelmoula, M.; Aissa, R.; Medjahdi, G.; Brunelli, M.; François, M. Aluminium Substitution in iron(II−III)-Layered Double Hydroxides: Formation and Cationic Order. *J. Solid State Chem.* **2008**, *181*, 2285−2291.
(7) Grégoire, B.; Ruby, C.; Carteret, C. Structural Cohesion of MII-MIII Layered Double Hydroxides Crystals: Electrostatic Forces and Cationic Polarizing Power. *Cryst. Growth Des.* **2012**, *12*, 4324−4333.
(8) Boclair, J. W.; Braterman, P. S. Layered Double Hydroxide Stability. 1. Relative Stabilities of Layered Double Hydroxides and Their Simple Counterparts. *Chem. Mater.* **1999**, *11*, 298−302.
(9) Hu, F.; Lin, S.; Li, P.; Yu, J. Quantitative Effects of Desorption Intensity on Structural Stability and Readsorption Performance of Lithium/Aluminum Layered Double Hydroxides in Cyclic Li+ Extraction from Brines with Ultrahigh Mg/Li Ratio. *Ind. Eng. Chem. Res.* **2020**, *59*, 13539−13548.
(10) Zhong, J.; Lin, S.; Yu, J. Effects of Excessive Lithium Deintercalation on Li+ Adsorption Performance and Structural Stability of Lithium/aluminum Layered Double Hydroxides. *J. Colloid Interface Sci.* **2020**, *572*, 107−113.
(11) Yan, G.; Wang, M.; Hill, G. T.; Zou, S.; Liu, C. Defining the Challenges of Li Extraction with Olivine Host: The Roles of Competitor and Spectator Ions. *Proc. Natl. Acad. Sci. U. S. A.* **2022**, *119*, No. e2200751119.
(12) Besserguenev, A. V.; Fogg, A. M.; Francis, R. J.; Price, S. J.; O'Hare, D.; Isupov, V. P.; Tolochko, B. P. Synthesis and Structure of the Gibbsite Intercalation Compounds [LiAl2(OH)6]X {X = Cl, Br, NO3} and [LiAl2(OH)6]Cl·H2O Using Synchrotron X-Ray and Neutron Powder Diffraction. *Chem. Mater.* **1997**, *9*, 241−247.
(13) Britto, S.; Kamath, P. V. Polytypism in the Lithium−Aluminum Layered Double Hydroxides: The [LiAl2(OH)6]+ Layer as a Structural Synthon. *Inorg. Chem.* **2011**, *50*, 5619−5627.
(14) Zhitova, E. S.; Pekov, I. V.; Chaikovskiy, I. I.; Chirkova, E. P.; Yapaskurt, V. O.; Bychkova, Y. V.; Belakovskiy, D. I.; Chukanov, N. V.; Zubkova, N. V.; Krivovichev, S. V.; Bocharov, V. N. Dritsite, Li2Al4 (OH) 12Cl2\textperiodcentered 3H2O, a New Gibbsite-Based Hydrotalcite Supergroup Mineral. *Minerals* **2019**, *9*, 492.
(15) Bookin, A. S.; Drits, V. A. Polytype diversity of the hydrotalcite-like minerals I. Possible polytypes and their diffraction features. *Clays and Clay Minerals* **1993**, *41*, 1.
(16) Bookin, A. S.; Drits, V. A. Polytype diversity of the hydrotalcite-like minerals II. Determination of the polytypes of experimentally studied varieties. *Clays and Clay Minerals* **1993**, *41*, 558.
(17) Sławiński, W. A.; Sjåstad, A. O.; Fjellvåg, H. Stacking Faults and Polytypes for Layered Double Hydroxides: What Can We Learn from Simulated and Experimental X-Ray Powder Diffraction Data? *Inorg. Chem.* **2016**, *55*, 12881−12889.
(18) Wypych, F.; De Freitas, R. A. Chapter 10 - Layered Double Hydroxides and Hydroxide Salts: Structure and Properties. In *Developments in Clay Science*; Wypych, F., De Freitas, R. A., Eds.; Elsevier, 2022; Vol. *10*, pp. 317−350.
(19) Whittaker, M. L.; Ren, D.; Ophus, C.; Zhang, Y.; Gilbert, B.; Waller, L.; Banfield, J. F. Ion complexation waves emerge at the curved interfaces of layered minerals. *Nat. Commun.* **2022**, *13*, 3382.
(20) Bourg, I. C.; Lee, S. S.; Fenter, P.; Tournassat, C. Stern Layer Structure and Energetics at Mica−Water Interfaces. *J. Phys. Chem. C* **2017**, *121*, 9402−9412.
(21) Jiménez-Ángeles, F.; Harmon, K. J.; Nguyen, T. D.; Fenter, P.; Olvera de la Cruz, M. Nonreciprocal Interactions Induced by Water in Confinement. *Phys. Rev. Res.* **2020**, *2*, No. 043244.
(22) Boyd, S.; Ganeshan, K.; Tsai, W.-Y.; Wu, T.; Saeed, S.; Jiang, D.-E.; Balke, N.; van Duin, A. C. T.; Augustyn, V. Effects of Interlayer Confinement and Hydration on Capacitive Charge Storage in Birnessite. *Nat. Mater.* **2021**, *20*, 1689−1694.
(23) Sassi, M.; Chaka, A. M.; Rosso, K. M. Ab Initio Thermodynamics Reveals the Nanocomposite Structure of Ferrihydrite. *Commun. Chem.* **2021**, *4*, 134.
(24) Yuwono, V. M.; Burrows, N. D.; Soltis, J. A.; Do, T. A.; Lee Penn, R. Aggregation of Ferrihydrite Nanoparticles in Aqueous Systems. *Faraday Discuss.* **2012**, *159*, 235.
(25) Sassi, M.; Rosso, K. M. Ab Initio Evaluation of Solid-State Transformation Pathways from Ferrihydrite to Goethite. *ACS Earth Space Chem.* **2022**, *6*, 800−809.
(26) Legg, B. A.; Zhu, M.; Comolli, L. R.; Gilbert, B.; Banfield, J. F. Determination of the Three-Dimensional Structure of Ferrihydrite Nanoparticle Aggregates. *Langmuir* **2014**, *30*, 9931−9940.
(27) Ren, D.; Ophus, C.; Chen, M.; Waller, L. A Multiple Scattering Algorithm for Three Dimensional Phase Contrast Atomic Electron Tomography. *Ultramicroscopy* **2020**, *208*, No. 112860.
(28) Ren, D.; Whittaker, M.; Ophus, C.; Waller, L. Distributed Reconstruction Algorithm for Electron Tomography with Multiple-Scattering Samples. *arXiv [physics.comp-ph]*, **2021**. http://arxiv.org/abs/2110.07857. (accessed 2022-12-10)
(29) Fernandez-Martinez, A.; Tao, J.; Wallace, A. F.; Bourg, I. C.; Johnson, M. R.; De Yoreo, J. J.; Sposito, G.; Cuello, G. J.; Charlet, L. Curvature-Induced Hydrophobicity at Imogolite−water Interfaces. *Environ. Sci.: Nano* **2020**, *7*, 2759−2772.
(30) Shimizu, S.; Matubayasi, N. Cooperative Sorption on Porous Materials. *Langmuir* **2021**, *37*, 10279−10290.
(31) Neupane, G.; Wendt, D. S. Assessment of Mineral Resources in Geothermal Brines in the US. In *Proceedings of the 42nd Workshop on Geothermal Reservoir Engineering*, Stanford University: Stanford, CA, USA; 2017; pp. 13−15.
(32) Sheng, A.; Liu, J.; Li, X.; Qafoku, O.; Collins, R. N.; Jones, A. M.; Pearce, C. I.; Wang, C.; Ni, J.; Lu, A.; Rosso, K. M. Labile Fe(III) from Sorbed Fe(II) Oxidation Is the Key Intermediate in Fe(II)-Catalyzed Ferrihydrite Transformation. *Geochim. Cosmochim. Acta* **2020**, *272*, 105−120.
(33) Sudare, T.; Ueda, M.; Yamaguchi, T.; Tipplook, M.; Tanaka, H.; Hayashi, F.; Teshima, K. Layer-Stacking Sequence Governs Ion-

Storage in Layered Double Hydroxides. *J. Phys. Chem. Lett.* **2023**, *14*, 584−591.

https://doi.org/10.1021/acs.chemmater.3c00072
Chem. Mater. 2023, 35, 3931−3940